Design and Optimization of a Magnetron DC–DC Isolated Power Supply With High Efficiency

Junkun Zhang, Bing Gao, Zhixing He, *Member, IEEE*, Lei Wang, *Senior Member, IEEE*, Renjie Hou, Yang Liu, An Luo, *Senior Member, IEEE*, Yandong Chen, *Senior Member, IEEE*, and Rong Han, *Student Member, IEEE*

***Abstract*—High-efficiency high voltage dc power supply is the core equipment for magnetron in the microwave industry. This article presents an input-parallel output-serial modular high isolated resonant converter for the magnetron. However, the high stray capacitance of the high isolation transformer brings some challenges, such as high turn-OFF current, longer dead time, increasing gain, and transformer optimization. A simplified model including the stray capacitances is built to deal with these problems, and the minimum turn-OFF current is derived after the detailed time-domain analysis. The appropriate deadtime and the maximum magnetic inductance needed for the proposed converter are obtained with the minimum turn-OFF current. Then, a 15 kW, 60 kV isolation multiple-windings output transformer is designed and optimized for the converter. The insulation design, core shape, losses, and parasitic parameters are calculated thoroughly. The Pareto optimization process optimizes the switching frequency and the transformer's turns to obtain higher efficiency and a more stable gain. The finite element method and time-domain simulation verified the optimized design results. Finally, a 0.8/2.5 kV, 15 kW all-SiC dc–dc converter module is developed to validate the proposed design. The results indicate that the module efficiency is as high as 98.6%.**

***Index Terms*—Input-parallel output-serial (IPOS), *LLC* converter, magnetron power supply, multioutput transformer.**

I. Introduction

THE high-efficiency, high-power magnetron power supply is widely used in various industrial applications such as food heating, smelting, meteorology, and other fields. Recently, since the better quality of the heated product without emissions, significant attention has been drawn to the application of industrial magnetrons. However, low efficiency and high device pressures hinder its higher voltage and power applications.

Due to the limitations of commercial switching devices, academic researchers have mainly concentrated on consumer-grade of the low voltage and power (<10 kV/10 kW) microwave magnetron studies [1]–[5]. The high voltage and power of industrial magnetron applications (>10 kV/50 kW) are barely reported in the literature.

However, these microwave magnetron of low voltage and power studies [2]–[5] are still beneficial for better efficiency. Most of these power supplies have been used as phase-shifted full-bridge (PSFB) and resonant converters to improve the efficiency and switching frequency. Furthermore, for the high voltage and high power applications, the modular combined converter with the input-parallel output-serial (IPOS) [6]–[11] are well-acknowledged to reduce the stresses of switching devices.

As far as the current literature on IPOS structures is concerned, most use DAB or PSFB as a module [6]–[9]. However, DAB is often used for bidirectional power flow due to its symmetrical structure. The PSFB has high losses and voltage spikes for its inability to achieve zero-current-switching (ZCS) on the secondary side. The *LLC* converter is employed to have soft-switching conditions for the secondary side [10] and [11]. Thus, it can achieve maximum efficiency of 97.5%. However, the experiment results are down-scaled with 3.6 kW and 1.2 kV. This high efficiency may lose for the high voltage and power application because of the unique resonant module design and potential significant parasitic parameters.

Inside the module, the converter is usually fed by a stable dc bus provided by Vienna or PWM rectification. They can provide a stable input voltage in the magnetron power supply. Therefore, the resonant converter can take the unregulated dc–dc transformer as an isolated stage to improve efficiency and simplify the control. Among the common resonant converters, they can be divided into series-resonant converter (SRC) [12] and [13], parallel-resonant converter (PRC) [14] and [15], *LLC* converter [18] and [19], and *LCC* converter [20]–[22]. SRC has a simple structure and high efficiency. However, zero-voltage-switching (ZVS) of turn-ON may lose at the resonant frequency. Besides, the PRC and *LCC* are widely used in high voltage applications. However, the efficiency varies greatly with the load. Recently, *LLC* topologies have been well developed in step-down applications [16]–[19]. They both provide a detailed analysis of loss and gain. However, when extended to the high ratio applications, the effect of stray capacitance due to junction capacitance and transformer cannot be ignored. Therefore, analysis and modeling of *LLC* converters containing stray capacitance are required.

Manuscript received December 13, 2021; revised February 13, 2022; accepted February 24, 2022. Date of publication March 1, 2022; date of current version April 28, 2022. This work was supported in part by the National Natural Science Foundation of China under Grant 52177180 and in part by the Hunan Natural Science Foundation under Grant 2021JJ20014. Recommended for publication by Associate Editor A. Safaee. *(Corresponding authors: Zhixing He.)*

The authors are with the College of Electrical and Information Engineering, Hunan University, Changsha 410082, China (e-mail: junkunzhang@hnu.edu.cn; gbdnbh@hnu.edu.cn; hezhixing@hnu.edu.cn; jordanwanglei@hnu.edu.cn; rjhou@hnu.edu.cn; liu_yang@hnu.edu.cn; an_luo@hnu.edu.cn; yandong_chen@hnu.edu.cn; hanrong@hnu.edu.cn).

Color versions of one or more figures in this article are available at https://doi.org/10.1109/TPEL.2022.3155257.

Digital Object Identifier 10.1109/TPEL.2022.3155257

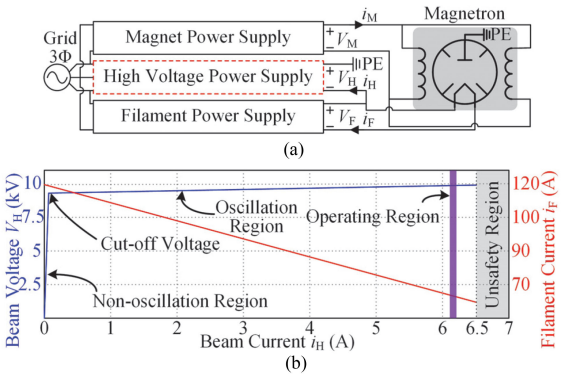

Fig. 1. Industrial magnetron of (a) power supply connection and (b) load characteristics.

The high-frequency high-voltage transformer is essential for the isolation and lifting voltage. Most literature focuses on parasitic parameters, efficiency, and gain [23]–[27]. Moreover, although most high-frequency transformers are used for step-down applications, detailed research has been carried out on winding and core losses [23] and [24], winding structure [25] and [26], and insulation [27]. However, the literature has rarely mentioned an analytical approach for step-up transformers in high-frequency, high-voltage, and high-power IPOS converters. Furthermore, the parasitic parameters are worth paying attention to the influence of the resonant converter operation. Besides, The leakage inductances for a 2-D based model are presented in [27], while the capacitance parameters are precisely extracted [28]. However, they cannot be used directly since this paper focuses on high-insulation, high-frequency, and high-power transformers.

The main contributions can be summarized as follows.

1) Equivalent time-domain equations of *LLC* converter are proposed considering the stray and junction capacitances. The equations can obtain critical conditions with the ZVS turn-ON conditions for the MOSFETs. It provides the necessary conditions for the overall optimization of the converter design.
2) In order to achieve a high voltage output with the utilization of the 1200 V SiC SBD diodes, a multiple output windings transformer is proposed, requiring high insulation on the primary and secondary sides. Calculating equations in which the leakage inductance and the parasitic capacitance can be unified into the time domain equation are proposed.
3) Due to the complexity of the design variables, the relationship corresponding to the combined transformer and converter design has the uncertainty of the target. Hence, the Pareto method is introduced to optimize efficiency and gain by unifying the relationship between the time-domain equation and transformer. Besides, the optimization result is validated by simulation and experiment.

The rest of this article is organized as follows. The topology and operation with stray capacitance are presented in Section II. Section III illustrates the crucial transformer model and its key parameters. A Pareto optimization process is given in Section IV

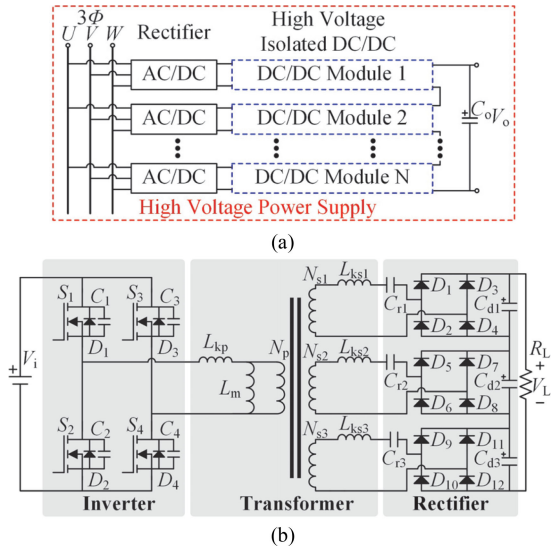

Fig. 2. High voltage power supply of (a) IPOS structure and (b) proposed basic module.

and verified by the finite element method (FEM) simulation. Then, Section V presents the experimental results and some discussions. Finally, Section VI concludes this article.

II. Operation of the Proposed Converter Module

Fig. 1(a) shows a graphic representation of the magnetic power supply. The cathode needs a filament power supply for heating. The output power is controlled by the magnetic field power supply and the filament power supply. The high voltage power supply is crucial to supply the high voltage energy. From load characteristics in Fig. 1(b), V_{H}'s fluctuation range is minimal for the operating region.

A. Modeling of the Module

As shown in Fig. 2(a), the high voltage power supply can be designed as the IPOS structure, accompanied by the advantages described in the introduction.

The essential element is the dc–dc module stage to lift and isolate voltage in Fig. 2(b). It includes an inverter, an HF transformer, and a rectifier. Each module is connected by way of IPOS. The APF rectifier acts as a preregulator to slightly regulate the output voltage.

Meanwhile, the inverter is a full bridge connected with the transformer. It is a one-winding input and three-windings output structure. C_{p} and L_{kp} are the stray capacitance and leakage inductance on the primary side.

($C_{\mathrm{s1}}, C_{\mathrm{s2}}, C_{\mathrm{s3}}$) and ($L_{\mathrm{k1}}, L_{\mathrm{k2}}, L_{\mathrm{k3}}$) are the stray capacitors and leakage inductances on the secondary side. L_{m} is the magnetic inductance. Besides, the rectifier is composed of three full diode bridges connected in series. The resonant capacitors (C_{r1}, C_{r2}, C_{r3}) connect to the input side of the transformer. Furthermore, the switching devices (S_1 –S_4) are SiC MOSFETs. The diodes (D_1–D_{12}) use SiC-SBD diode with junction capacitors C_{doss} and do not reverse recovery.

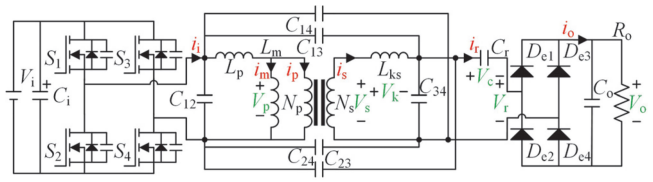

Fig. 3. Equivalent HF transformer and resonant circuit.

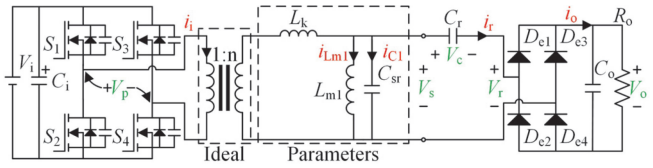

Fig. 4. Simplified HF transformer and resonant circuit.

As for the transformers, it needs to realize the output voltage sharing for each secondary winding. A suitable transformer solution for the output voltage sharing is given in Section III. Furthermore, the imbalance caused by leakage inductance is given in Appendix A. Moreover, with the proposed transformer, the output parameters of each winding are uniform.

Hence, the transformer parameters can be regarded as equal as

$$\begin{aligned} &N_{s1}{=}N_{s2}{=}N_{s3}{=}N_s/3 \;\; L_{ks1}=L_{ks2}=L_{ks3}{=}L_{ks}/3 \\ &N_p:N_s{=}n \;\; C_{r1}=C_{r2}=C_{r3}{=}3C_r \;. \end{aligned} \tag{1}$$

Based on the abovementioned equivalent, three secondary windings are equivalent to one winding, as shown in Fig. 3.

Based on the two-port approach, the primary side parameters are converted to the secondary side shown in Fig. 4. Since L_m is larger than $L_p{+}L_{ks}$, the equivalent values can be obtained as follows:

$$\begin{aligned} &L_k=n^2L_p+L_{ks} \;\; L_{m1}=n^2L_m \\ &C_{sr}=C_{12}/n^2{+}C_{34}+(1-1/n)^2\,(C_{13}{+}C_{24}-C_{14}-C_{23})\,. \end{aligned} \tag{2}$$

Since the converter gain is an important performance, the fundamental harmonic approximation (FHA) method is used considering the stray capacitance. The gain M of the converter can be calculated as follows:

$$M{=}\,1/\left\langle \begin{array}{l} 1+j\,(\omega L_k-1/(\omega C_r))\,/R_{eq}{+} \\ j\omega L_k\,\{1+j\,(\omega C_{sr}-1/\omega L_{m1})\,[1-j\,(1/\omega C_rR_{eq})]\} \end{array} \right\rangle \tag{3}$$

where R_{eq} is the equivalent resistance equaling $8n^2R_o/\pi^2$.

In the converter design, it is expected that M varies as small as possible with R_{eq}, realizing a wide load output range.

According to (3), the better gain characteristics can be obtained with the larger L_{m1}, the smaller C_{sr}, and the switching frequency f_s closer to ω_r.

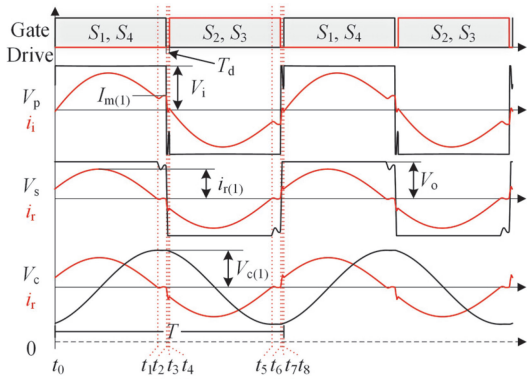

Fig. 5. Switching patterns, main voltage waveforms, and main output waveforms of equivalent HF transformer and resonant circuit.

B. Operation of the Module

Fig. 5 shows the main waveforms for the steady-state operating conditions. The switching sequences divide into eight modes. Since the first half-cycle period is symmetrical to the latter half-cycle, the whole operation analysis is replaced by the first half-cycle.

Mode 1 [$t_0 \le t < t_1$]: First, S_1 and S_4 switch ON at t_0. Since the impedance values of L_{m1} and C_{sr} are large, at this time, the resonance is mainly caused by L_k and C_r.

The voltage $n\,V_i$ and V_o apply to L_k and C_r. V_c is then calculated as

$$\begin{aligned} &V_c\,(t-t_0)=\left(-V_{C(1)}-nV_i+V_o\right)\cos\omega_r\,(t-t_0) \\ &+\left[I_{m(1)}/\left(n\omega_rC_r\right)\right]\sin\omega_r\,(t-t_0)+nV_i-V_o \end{aligned} \tag{4}$$

where $Z_r=\sqrt{L_k/C_r}$ and $\omega_r=1/\sqrt{L_kC_r}$.

i_r expresses as

$$\begin{aligned} &i_r\,(t-t_0)=\left(V_{C(1)}+nV_i-V_o\right)C_r\omega_r\sin\omega_r\,(t-t_0) \\ &+\left(I_{m(1)}/n\right)\cos\omega_r\,(t-t_0)\,. \end{aligned} \tag{5}$$

Mode 1 ends when i_r becomes zero.

Then, the duration time t_{01} expresses as

$$t_{01}{=}\frac{1}{\omega_r}\arctan\frac{-\left(I_{m(1)}/n\right)}{C_r\left(V_{C(1)}+nV_i-V_o\right)\omega_r}. \tag{6}$$

Since the only i_r transmits energy in the whole period, P_{out} can be calculated as

$$P_{out}{=}\,2f_sV_o\int_0^{t_{12}}i_r\mathrm{d}t{=}\,4f_sV_oC_rV_{C(1)}. \tag{7}$$

Mode 2 [$t_1 \le t < t_2$]: Mode 2 starts when i_r becomes zero. Then, i_i continues to increase linearly. Since L_{m1} is much larger than L_k, i_{Lm1} is mainly determined by the input voltage V_i and switching frequency f_s.

This mode ends at t_2 when i_i reaches $I_{m(1)}$. $I_{m(1)}$ expresses as

$$I_{m(1)}{=}V_i\,(1/f_s-2T_d)\,/\,(4L_m) \tag{8}$$

where T_d is the deadtime.

i_{Lm} can be expressed as

$$i_{Lm}\,(t-t_0)=-\,I_{m(1)}+2I_{m(1)}\,(t-t_0)\,. \tag{9}$$

Mode 3 [$t_2 \le t < t_3$]: Mode 3 starts when S_1 and S_4 turn OFF.

Then, i_i starts to discharge capacitors C_1 and C_4, to charge C_2 and C_3. i_i can be expressed as

$$i_\mathrm{i}(t-t_2) = 2C_\mathrm{oss}\begin{pmatrix} -C_1\omega_1 \sin\omega_1 t' + C_2\omega_1\cos\omega_1 t' \\ -\left(3A_3t'^2 + 2A_4t' + A_5\right)/A_2 \end{pmatrix} \quad (10)$$

where $t - t_2 = t'$; C_oss is the output capacitance of the MOSFETs; C_doss is the output capacitance of diodes. Since C_doss is much smaller than C_oss, the diode is assumed to complete the charging process. Appendix B shows the remaining parameters. Here, the voltage V_Mc1 of C_1 can be expressed as

$$\begin{aligned} V_\mathrm{Mc1}(t-t_2) =& C_1\cos\omega_1 t' + C_2\sin\omega_1 t' \\ &-\left(A_3t'^3 + A_4t'^2 + A_5t' + A_6\right)/A_2. \end{aligned} \quad (11)$$

i_r can be expressed based on V_Mc1 as

$$i_\mathrm{r}(t-t_2) = \begin{pmatrix} (1/L_\mathrm{m})\int (V_\mathrm{i} - 2V_\mathrm{Mc1})\mathrm{d}t' + I_{m(1)} \\ -2\left(C_\mathrm{oss} + n^2C_\mathrm{sr}\right)(\mathrm{d}V_\mathrm{Mc1}/\mathrm{d}t') \end{pmatrix}/n. \quad (12)$$

When $V_\mathrm{doss}(t+t_\mathrm{p1}) = V_\mathrm{o}$ - $V_\mathrm{c(1)}/2$, the mode of the first half is completed. At this time, $I_{m(2)} = I_{m(1)} + (1/L_\mathrm{m})\int_0^{t_\mathrm{p1}}(V_\mathrm{i} - 2V_\mathrm{c})\mathrm{d}t$, $V_\mathrm{Mc12} = V_\mathrm{Mc1}(t_\mathrm{p1} + t_2)$, and $I_\mathrm{r2} = i_\mathrm{r}(t_\mathrm{p1} + t_2)$.

When the charge of C_doss is completed, $V_\mathrm{r} = -V_\mathrm{o}$. Here, the voltage V_Cd can be expressed as $V_\mathrm{Cd} = (1/C_\mathrm{doss})\int i_\mathrm{r}/2\mathrm{d}t$.

Then, the mode of the last half is completed when V_Mc1 becomes V_i. The duration should satisfy the relation

$$\begin{aligned} &C_3\cos\omega_2 t_\mathrm{p2} + C_4\sin\omega_2 t_\mathrm{p2} \\ &-\frac{B_3{t_\mathrm{p2}}^3 + B_4{t_\mathrm{p2}}^2 + B_5t_\mathrm{p2} + B_6}{B_2} = V_\mathrm{i}. \end{aligned} \quad (13)$$

If i_i does not reach zero at this time, resonance occurs through L_k and C_r, and S_2 and S_3 can be turned ON with ZVS.

Mode 4 [$t_3 \le t < t_4$]: Mode 4 starts when i_i becomes zero. However, this mode leads to a loss of ZVS in turn ON.

In general, the energy is transferred to the load in *mode 1*. Furthermore, *Mode 2* is desired as short as possible to reduce processes because this mode does not transfer energy. Besides, it is expected that the turn ON of ZVS is implemented in Mode 3 without Mode 4.

The condition for achieving ZVS in turn ON is

$$(1/L_\mathrm{m})\left((1/f_\mathrm{s}) - T_\mathrm{d}\right)^2 > 64\left(C_{oss} + C_\mathrm{sr}n^2 + n^2C_\mathrm{doss}\right). \quad (14)$$

Besides, T_d needs to meet (15) as

$$T_\mathrm{d} > t_\mathrm{p1} + t_\mathrm{p2}. \quad (15)$$

When the MOSFET is turned OFF, the stray capacitor C_sr and C_doss flow a portion of the turn-OFF current, which reduces the conditions for the MOSFET to achieve ZVS. Therefore, it requires an increase in the turn-OFF current.

The conditions for the implementation of ZVS are given in (14) and (15). However, since the transcendental equation is involved, the authors use the numerical solution of the fsolve function in MATLAB to solve t_p1, t_p2, and L_m for soft switching realization.

C. Efficiency of the Module

Efficiency is a crucial indicator for a module. The efficiency can be evaluated when the B part establishes the time-domain equations. First, the efficiency η can be calculated by losses P_sumloss and output power P_out as

$$\eta = P_\mathrm{out}/\left(P_\mathrm{out} + P_\mathrm{sumloss}\right). \quad (16)$$

Since the P_out for a single module has been specified for a high power as 15 kW, the key is to calculate the total loss P_sumloss for efficiency calculation. Since P_out is high, Some more minor losses can be ignored, such as drive losses. Hence, the primary considerations are the H-bridge turn-ON loss $P_\mathrm{mos\_ON}$, the MOSFET turn-OFF loss P_MOSOFF, the rectifier bridge loss P_Diode, the transformer copper loss P_Iloss, and the transformer core loss P_Closs.

Hence, the sum loss P_sumloss can be expressed as

$$P_\mathrm{sumloss} = P_\mathrm{Mos\_on} + P_\mathrm{MOSoff} + P_\mathrm{Diode} + P_\mathrm{Iloss} + P_\mathrm{Closs}. \quad (17)$$

Furthermore, the H-bridge turn-ON loss $P_\mathrm{mos\_ON}$ can be expressed as

$$P_\mathrm{Mos\_on} = 4f_\mathrm{s}R_\mathrm{DS\_ON}\int_{t_0}^{\frac{1}{2f_\mathrm{s}}} {i_\mathrm{i}(t)}^2\mathrm{d}t. \quad (18)$$

The turn-OFF losses of the switching devices are estimated. The current, which flows to the MOSFETs is regarded as a linear decrease. Then, the turn-OFF losses P_MOSOFF can be expressed as

$$P_\mathrm{MOSoff} = \frac{1}{12C_\mathrm{oss}}{I_{m(1)}}^2{t_\mathrm{f}}^2f_\mathrm{s} \quad (19)$$

where t_f is the turn-OFF time of the MOSFETs.

For the rectifier bridge loss, it can be expressed as

$$P_\mathrm{Diode} = 12f_\mathrm{s}V_\mathrm{f}\int_{t_0}^{\frac{1}{2f_\mathrm{s}}} i_\mathrm{r}(t)\mathrm{d}t. \quad (20)$$

The transformer copper loss and the transformer core loss can be calculated next. With these expressions, the efficiency can be expressed.

III. Analysis of the Transformer

A. Modeling of the Transformer

In order to illustrate the characteristics of the transformers, representative transformers with sectional secondary outputs are selected. As shown in Fig. 6, the comparisons are shown under the voltage and current conditions.

As a comparison, the primary and secondary sides of the UU-type core around the core column produce a larger leakage field. The magnetic field distribution of the secondary windings is also uneven, especially in the middle one just in the middle of the air gap. As an improvement, the secondary windings in Fig. 6 are not close to the air gap. Furthermore, the leakage magnetic field on the left and right sides is significantly reduced. Although the structure of Fig. 6(b) is more uniform than Fig. 6(a), the induced magnetic field of the secondary winding is also challenging to achieve uniformity. Besides, since the winding surrounds the

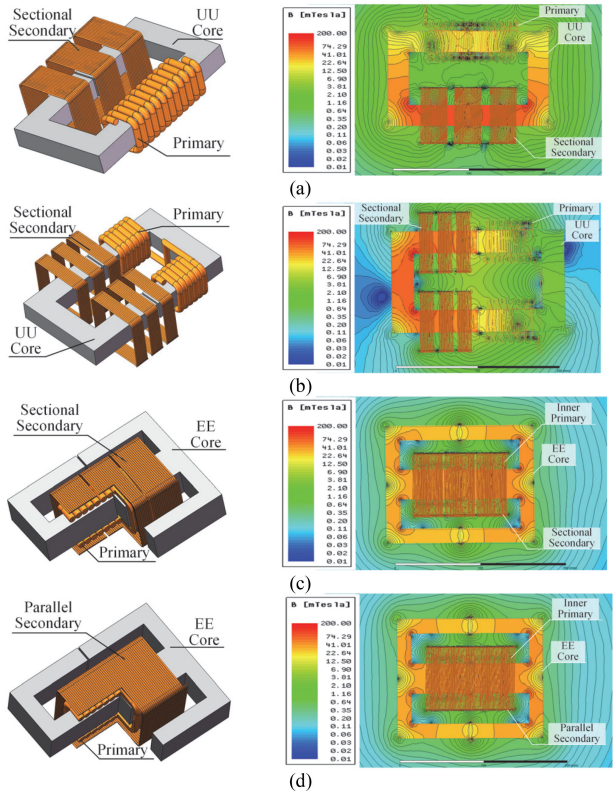

Fig. 6. Magnetic field simulation comparison of in (a) UU core with the primary winding and the separated secondary multiwindings, wound of on separated legs [29]. (b) UU core with the primary winding and the separated secondary multiwindings, wound of on separated cores [27]. (c) EE core with the primary winding and the separated secondary multiwindings, wound of on middle leg [30]. (d) EE core with the primary winding and the parallel secondary multiwindings, wound of on middle leg, when excitation current equals 18.75 A in the primary winding and 6 A in the secondary windings.

core tightly, the requirement for core heat dissipation of the UU core is high.

As for the EE-type cores, the leakage field is mainly confined between the primary and secondary sides, allowing for smaller leakage inductance and higher transformer efficiency. However, the secondary side of Fig. 6(c) is wound in sections, which leads to uneven distribution of the induced magnetic field to the secondary windings.

Based on the abovementioned results, this article adopts a transformer method with three strands of wires wound in parallel for the secondary side. It makes the induced magnetic field output from each winding uniform and, thus, achieves output voltage sharing for each winding.

When the magnetic core and structure are determined, Fig. 7 shows the proposed transformer. The primary winding surrounds the middle limb; thus, the secondary windings are easier to lead out with three parallel strands.

Then, each strand connects to a separate rectifier bridge. This approach makes the input voltage of each rectifier bridge uniform. Since the skin effect and the proximity effect of the windings, the Litz wire is utilized. Besides, choosing a long h_1 allows the winding to be wound in one layer, reducing the

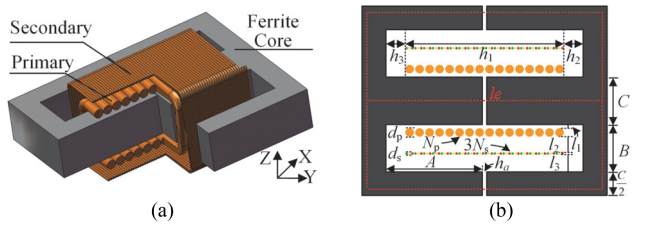

Fig. 7. Structure of the proposed transformer. (a) Three-dimensional geometry view. (b) Cross-sectional view.

proximity effect. As shown in Fig. 7(b), the size parameters between the magnetic core and the windings are marked.

Based on the symmetry, some principles limit the geometric dimensions of the transformer and are expressed by

$$\begin{aligned} &h_1 + h_2 + h_3 \le 2A + h_\mathrm{a}; \\ &3N_\mathrm{s}d_\mathrm{s} \le h_1; l_1 + l_2 + l_3 + d_\mathrm{s} + d_\mathrm{p} \le B. \end{aligned} \tag{21}$$

For the insulation distance, the limit is expressed by

$$l_2 \ge l_\mathrm{iso} \;\; l_3 \ge l_\mathrm{iso} \;\; h_2 = h_3 \ge 2l_\mathrm{iso} \tag{22}$$

where l_iso is the isolated distance considering the isolated voltage V_iso. Due to the consideration of the lead-out parts, h_2 and h_3 should be higher than l_iso.

Insulation materials are commonly used to obtain higher insulation voltage. There are some common insulation materials compared in [27]. Organic silicon is chosen as potting insulation material for its high dielectric strength and thermal conductivity. Besides, a rule of thumb is that the dielectric strength varies inversely with the thickness's 0.4 power [31].

The relationship between l_iso and V_iso expresses as

$$l_\mathrm{iso} = (V_\mathrm{iso}/V_\mathrm{ref})^{\frac{5}{3}} (1/l_\mathrm{ref})^{\frac{2}{3}} \tag{23}$$

where V_ref is reference dielectric strength under reference thickness l_ref.

B. Magnetic Modeling of the Transformer

The magnetic model is proposed to obtain magnetic strength and leakage inductance. Four assumptions are present to simplify the model as follows.

1) The ampere-turns $N_\mathrm{p}I_\mathrm{p}$ equals $N_\mathrm{s}I_\mathrm{s}$. This assumption makes no magnetizing or leakage flux in the core.
2) The permeability of the core is infinite. It makes the magnetic field strength become zero inside the core.
3) The skin effect and approximate effect are neglected due to the Litz wire and the single-layer windings.
4) The single layer is equivalent to the conductive foil. Fig. 8 shows the top-view profile of the simplified transformer to analyze the model with a 3-D view. The position can divide into six parts in the right half-plane from (a) to (f).

Hence, the top-view profile's magnetic field strength is related to the horizontal and core positions. Moreover, magnetic leakage energy is mainly stored in the windings, the gap between windings, and the windings and core. Hence, Leakage energy can be calculated.

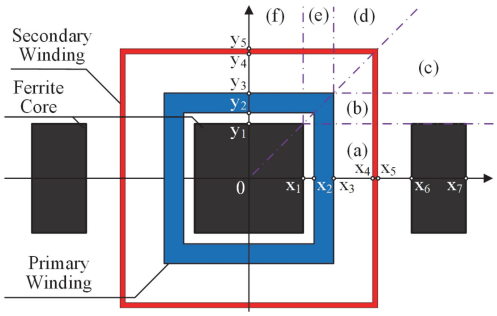

Fig. 8. Top-view profile of the transformer.

C. Calculating Parameters

This part focuses on calculating the vital parameters based on the transformer modeling.

1) Air Gap: The air gap h_a can reduce the core's relative permeability. L_m can be reduced by this method. Hence, the magnetizing inductance L_m can be controlled with the help of h_a

$$L_m = A_e {N_p}^2 \mu_0 \mu_r / (2h_a \mu_r + l_e) \tag{24}$$

where μ_r is the core's relative permeability; μ_0 is the air's permeability; l_e is the magnetic path without air gap; A_e is the effective cross-section of the core.

However, the increase in h_a cannot reduce the maximum magnetic flux density B_m. In contrast, it increases the copper loss of the primary winding. Therefore, h_a should adjust L_m so that it just reaches the ZVS condition.

2) Winding Turns: Considering the magnetic saturation, the primary winding turn N_p is limited by

$$N_P = V_i / (4.44 f_s B_m A_e). \tag{25}$$

3) Iron Losses: A detailed comparison with arbitrary excitation is presented [32]. The rectangular modified extension steinmetz equation has high accuracy in the loss calculation.

The expression is given by

$$P_{lloss} = (8/\pi^2)^{\alpha-1} k {f_s}^{\alpha-1} {B_m}^{\beta} V_{EE} \tag{26}$$

where k, α, and β result from the manufacturer's curve fitting, and V_{EE} is the core volume.

4) Copper Losses: The skin effect reduces through Litz wire utilization in the proposed transformer. The proximity effect is neglected due to the single-layer winding. The copper losses are given by

$$P_{Closs} = 4F_r \rho_{cu} \left[\begin{array}{l} N_p \frac{C+2l_1+d_p}{S_{sp}} \frac{4}{T} \int_0^{\frac{T}{2}} {i_i}^2(t)\,dt \\ +nN_s \frac{C+2(l_1+l_2+d_p)+d_s}{S_{ss}} \frac{4}{T} \int_0^{\frac{T}{2}} {i_r}^2(t)\,dt \end{array} \right] \tag{27}$$

where F_r considers the skin effect and ρ_{cu} is the electrical resistivity of the wire. The S_{sp} and S_{ss} are the equivalent cross-sectional area of the Litz wire for the primary and secondary sides.

Calculating F_r is given in [33] with the Dowell formula. F_r presents as

$$F_r = \Delta \frac{\sinh(2\Delta) + \sin(2\Delta)}{cosh(2\Delta) - \cos(2\Delta)} \tag{28}$$

where $\Delta = d/\delta$, with the d as the Litz wire diameter and δ as the skin depth decided by the switching frequency.

5) Leakage Inductance: Leakage magnetic energy is calculated with the magnetic model in Part B and given in

$$W_m = \frac{1}{2}\mu_0 \int \left(4 \sum_{i=1}^{6} {H_i}^2 \right) dV. \tag{29}$$

W_m can also be expressed with L_k and I_s as

$$W_m = \frac{1}{2} L_k {I_s}^2. \tag{30}$$

Based on these, L_k can be calculated by (22) and (23), and the magnetic field strength. It can be expressed as

$$L_k = 4\mu_0 {N_s}^2 f(l_1, l_2, l_3, h_1, d_s, d_p) \tag{31}$$

where $f(l_1, l_2, l_3, h_1, d_s, d_p)$ is the function related to l_1, l_2, l_3, h_1, d_s, and d_p. Furthermore, $f(l_1, l_2, l_3, h_1, d_s, d_p)$ increases with l_1, l_2, and l_3. L_k is proportional to the square of N_s.

6) Stray Capacitance: A method calculating the stray capacitance is presented with a flat model [34]. The single-layer winding structure in this article can easily derive the capacitance parameters based on the model. However, some structures have complex electric field distribution, such as Fig. 6(a) and (b). The calculations of stray capacitance may have significant errors and require a more accurate method, such as the FEM. Moreover, a simplified model is given in [35]. Combing with (2), C_{sr} is then expressed by

$$C_{sr} = \left(\frac{1}{2n^2} - \frac{2}{3n} + \frac{1}{2} \right) \varepsilon_0 \varepsilon_r \frac{4h_1 [C + 2(l_1 + d_p)]}{l_2} \tag{32}$$

where ε_0 is the permittivity of the air and ε_r is the insulation material's relative permittivity.

IV. Design and Process of Optimum

A. Optimization Process

Based on the modeling of Sections II and III, the combined design and optimization of the transformer and converter are carried out. The relevant parameters and optimization goals are shown in Fig. 9. In this article, the design aims to optimize converter efficiency and voltage gain.

1) The module's parameters are present in Table I. V_i considers being equal to 800 V with the utilization of 1200 V SiC MOSFET.
2) According to (16), the insulation length l_{iso} is 8 mm with organic silicon for 60 kV isolation. Besides, 60 kV isolation makes the module compatible with high voltage and power level magnetron applications, up to 20 kV/120 kW. Since the voltage on the primary side is low, the magnetic core is close to the primary side. Then, l_{iso} must be smaller than l_2 and l_3 for the isolated design. Through the calculation, the size of the Litz wire is presented.

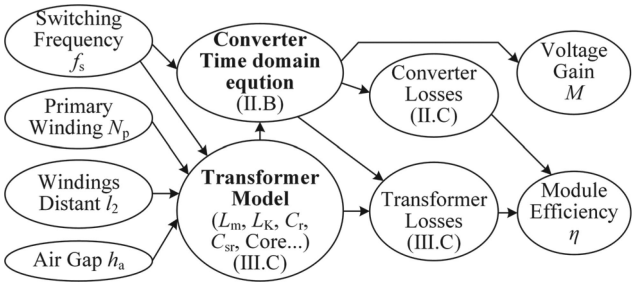

Fig. 9. Relationship of relevant parameters and optimization goals.

TABLE I
CALCULATION OF THE PROPOSED CONVERTER

Symbol	Quantity	Value
V_i	input voltage	800V (DC)
η_{min}	minimum efficiency	≥90% (≥25% rated power)
P_{out}	rated output power	15 kW for one module
V_{iso}	isolated voltage	60 kV
V_L	load voltage	2.5 kV
T_d	deadtime	= 250 ns
$L*W*H$	design module size	550*400*133 (mm)

TABLE II
PARAMETERS OF THE TRANSFORMER

Symbol	Value	Symbol	Value	Symbol	Value
h_1	d_p*N_p mm	l_2	>=8 mm	l_{iso}	8 mm
h_2	(138-h_1)/2mm	l_3	20 – l_2 mm	C	35 mm
h_3	(138-h_1)/2mm	A	69 mm	d_s	2 mm
l_1	5mm	B	35 mm	d_p	8 mm

Besides, The Litz wire of the primary and secondary sides is 0.1 mm × 2000 strands and 0.1 mm × 330 strands. The parameters of the transformer are shown in Table II. According to Fig. 10, these parameters can be used for multiobjective optimization after determining the dimension parameters. Based on (33), the copper loss due to the excitation current is much greater than the loss consumed in MOSFETs junction capacitance without the ZVS realization. However, L_m should not be small either. It will increase the turn-OFF current and cause excessive turn-OFF losses. Hence, the air gap h_a is used to control L_m just for achieving ZVS realization

$$\underbrace{\frac{1}{3}\rho_{cu}F_r N_p V_i^2 \frac{C+2l_1+d_p}{S_{sp}L_m^2 f_s^2}}_{\text{CopperLoss}} \leq\leq \underbrace{2C_{oss}V_i^2 f_s}_{\text{CapacitanceLoss}} \tag{33}$$

f_s, N_p, and l_2 are decision vectors. There are some limits based on the core, the insulation, and the switches. The goals are to optimize efficiency η and gain M. The mathematical expression

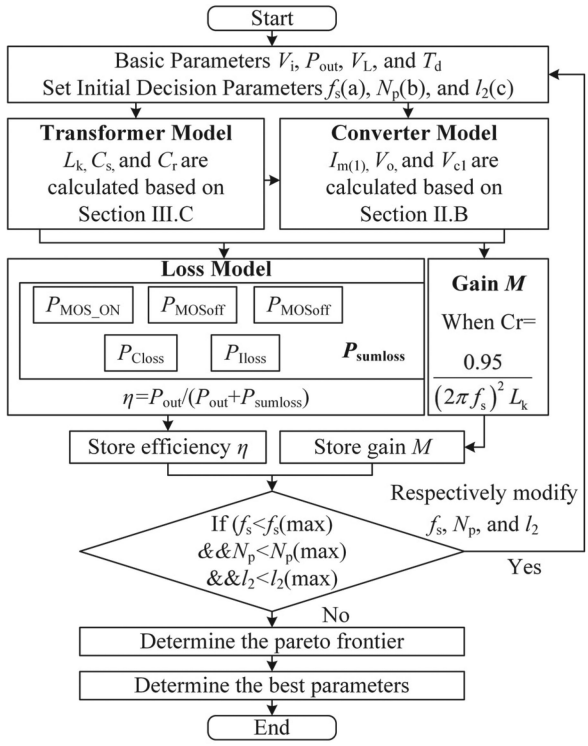

Fig. 10. Optimized design process.

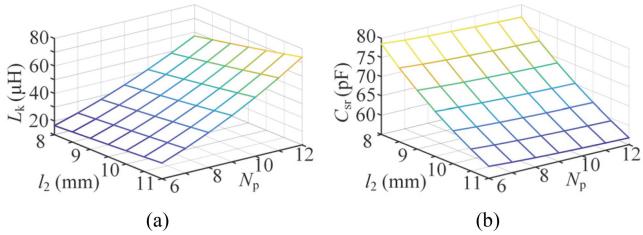

Fig. 11. Variation in L_k and C_{sr} with the variable of l_2 and N_p.

is as follows:

$$\begin{cases} \max \quad y = F(X) = (\eta(x), M(x))^T \\ \text{subjectto} \begin{cases} 50\,\text{kHz} \le f_s \le 125\,\text{kHz} \\ 6 \le N_p \le 12 \\ 8\,\text{mm} \le l_2 \le 11\,\text{mm} \end{cases} \\ \text{where} \quad X = [f_s, N_p, l_2]^T \end{cases}. \tag{34}$$

With the calculation of L_k and C_s, they are variable with N_p and l_2. Fig. 11 shows the figure of the L_k and C_{sr}.

Fig. 12 shows the efficiency η changing with f_s, l_2, and N_p. When f_s increases to 100 kHz, η is slightly increased due to the decrease of B_m.

However, when f_s rises, the frequency increases the iron loss. In this case, it is necessary to reduce the size of the core to reduce the core loss. However, the transformer volume cannot be further reduced due to insulation and core limitation. From the perspective of a single frequency, the decrease of l_2 increases the distributed capacitance, causing a decrease of η. N_p is a critical factor affecting the transformer. As N_p increases, η increases.

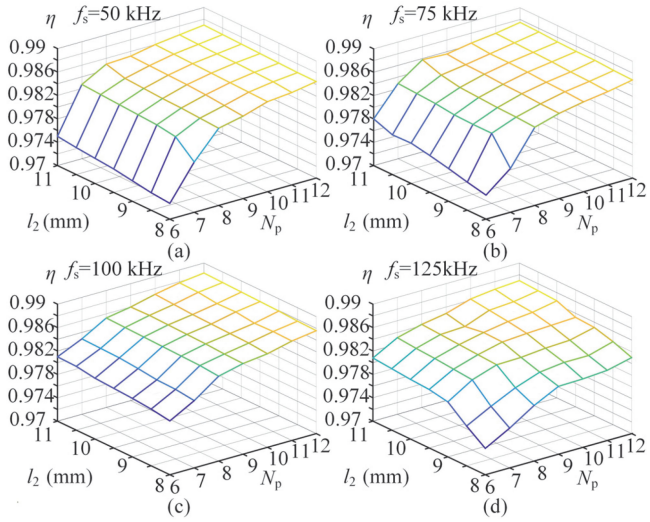

Fig. 12. Efficiency η in (a) $f_s = 50$ kHz, (b) $f_s = 75$ kHz, (c) $f_s = 100$ kHz, and (d) $P_{out} = 125$ kHz due to the variable of l_2 and N_p.

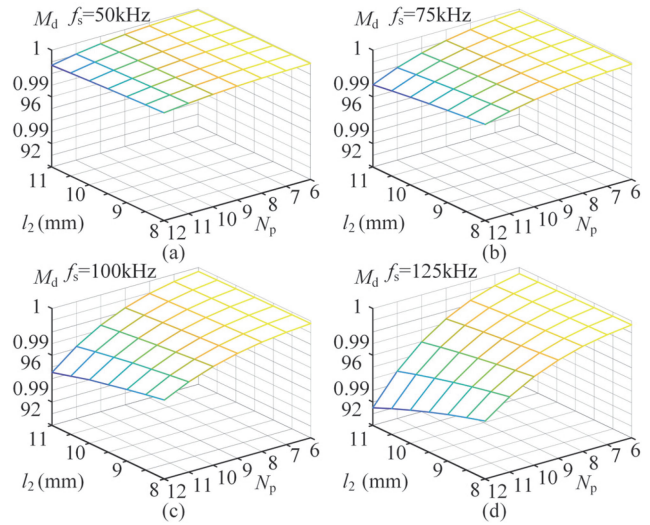

Fig. 13. Gain M in (a) $f_s = 50$ kHz, (b) $f_s = 75$ kHz, (c) $f_s = 100$ kHz, and (d) $P_{out} = 125$ kHz due to the variable of l_2 and N_p.

A bigger N_p can reduce B_m and thereby reduce core losses. Of course, if N_p increases without limit, it increases losses in the windings. At the same time, because bigger N_p requires a larger core, the core losses increase.

Since M is a curve that is not easy to measure intuitively, the gain value M is selected as the voltage gain characteristic when the capacitance C_r deviation is 15%. From Fig. 13, the gain M_d changes are limited due to the large equivalent impedance caused by step-up characteristics. Furthermore, as the f_s increases, M_d decreases due to the decrease of L_m. Furthermore, the more N_p, M_d becomes smaller due to the increase in L_k. Simultaneously, as l_2 decreases, the distribution capacitance becomes larger, which leads to an increase of M.

As shown in Fig. 10, by substituting the minimum of the three parameters to the given formula, the values of the individual

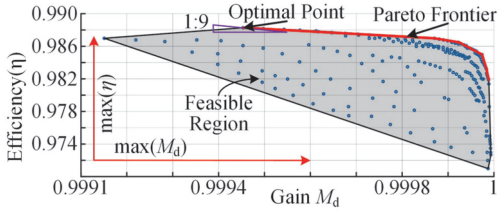

Fig. 14. Pareto optimized result.

TABLE III
CIRCUIT PARAMETERS OF THE ISOLATED TRANSFORMER

Symbol	Simulated Value	Calculated Value	Deviation of the value
L_m	190 μH	208 μH	8.6% ↓
L_k	59 μH	55 μH	6.78% ↑
C_{sr}	39 pF	41 pF	3.3% ↓

points can be solved. The obtained efficiency and gain values are saved. Furthermore, the M_d and η are calculated by varying the above three parameters with the variable of specific step values until these three parameters reach the maximum values.

Following this method, the point values can be plotted in Fig. 14. Moreover, the weight analysis method is adopted. The analysis is carried out according to the weight of 9:1 for considering that M varies over a narrow range. The optimal results are equal to 100 kHz, 12 turns, and 11 mm.

A. Simulated Verification

First, FEA simulation is used to verify the calculated parameters shown in Table III. In summary, compared to the simulated values, the errors in the calculated magnetic field values are mainly due to treating the permeability of the core as infinity, neglecting the edge flux generated by the air gap, and idealizing the magnetic circuit. The electric field calculation mainly equates the coils into a plane, idealizing the distribution of the electric field. The magnetic path's idealization results in a short magnetic flux path, resulting in a large calculated value for magnetic calculation. For leakage calculation, two main points further lead to the calculated value smaller than the simulated one: 1) The copper foil ignores the leakage inductance between turns. 2) The leakage inductance energy stored in the core and the transformer shell is ignored. However, the FEA method fails to reveal the intrinsic relationship with time-consuming and much computing resources.

Furthermore, the calculation and model presented have relatively high precision for design. To illustrate the advantages of the proposed transformer, the FEM simulation of the segmented windings is compared. The comparison results are shown in Table IV. The proposed transformer is more uniform than the segmented one from the results.

Fig. 15 shows the magnetic field distribution of the proposed transformer. The main leakage flux is in the space between the primary and secondary windings, consistent with the equivalent model. Through precise parameters obtained by the FEM simulation, the converter is verified by time-domain simulation.

TABLE IV
COMPARISON OF THE TRANSFORMERS

Mutual Inductor With Primary Side	Secondary Winding1	Secondary Winding2	Secondary Winding3
Proposed One	272 μH	273 μH	272 μH
Segmented Winding	269 μH	279 μH	269 μH

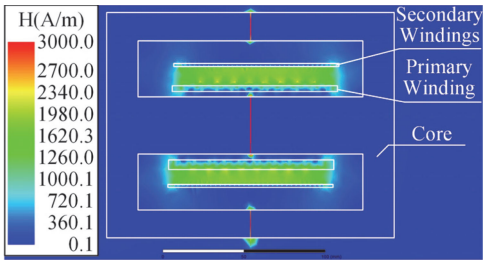

Fig. 15. Magnetic field distribution of the transformer when excitation current equals 18.75 A in the primary winding and 6 A in the secondary windings.

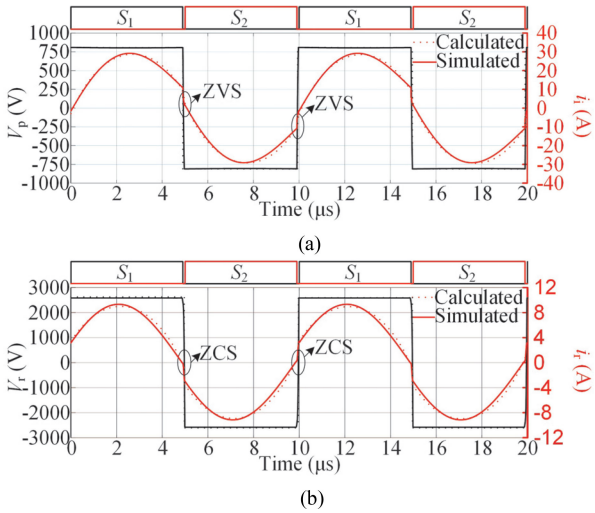

Fig. 16. Waveforms in (a) inverter and (b) rectifier when input voltage and output power equal to 800 V and 15 kW.

Fig. 16 shows the main voltage and current with the 800 V input and 15 kW output. The dotted line shows the waveforms of the computed model. The trend of both changes is the same.

B. Representative Topologies Simulated Comparison

The voltage and current levels compared in the literature are not consistent with the representative topologies. Therefore, Fig. 17 shows the representative topologies analysis by simulating the loss analysis.

Inverter losses, the frequency, and stray capacitance are optimized in this article compared to [11], resulting in lower turn-OFF losses of MOSFETs. The *LCC* resonant converter has a low turn-OFF loss due to the low turn-OFF current. However, the turn-ON losses are higher than the *LLC* converter due to charge shifting on the junction capacitance of the MOSFETs. Although the PSFB achieves ZVS, the turn-OFF loss is highest due to the high turn-OFF current.

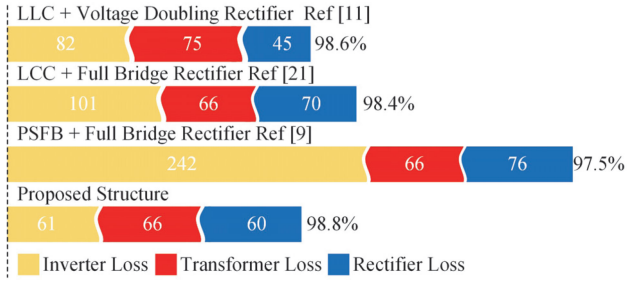

Fig. 17. Loss analysis of the representative topologies.

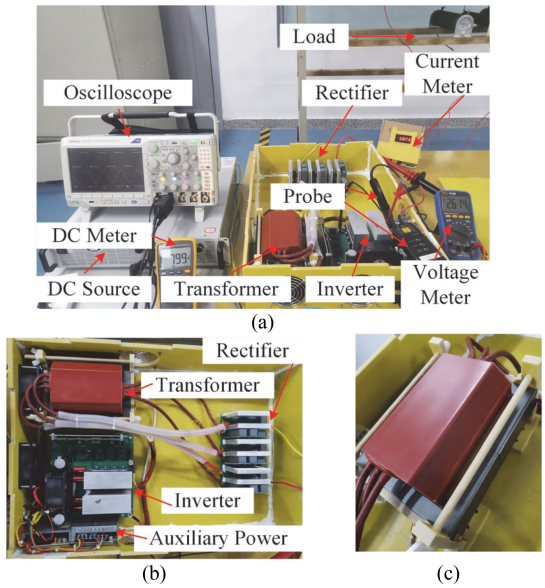

Fig. 18. Photograph of IPOS module prototype. (a) Test panorama. (b) Modules prototype hardware. (c) Transformer prototype.

Transformer losses, despite the increase of frequency to reduce the magnetic density in [11], the magnetic and copper losses caused by the proximity effect, skin effect increase simultaneously. In contrast, this makes the losses increase. While *LCC*, PSFB, and this article, losses are considered the same due to similar voltage and current in the transformer.

As for the voltage doubling rectifier, the number of diodes is reduced for the rectifier bridge losses. The boost ratio is double due to voltage doubling rectification. However, the output capacitance needs to be more significant. At the same time, the load cannot be high as full-bridge rectification. Nevertheless, voltage doubling rectification can be a way to reduce losses in some cases where the load is light.

After comparison, the model and design integrate the optimization of whole converter losses.

V. EXPERIMENTAL RESULTS

To verify the proposed converter's effectiveness, an experimental prototype has been implemented using 1200-V C2M0040120D SiC MOSFET and 1200-V SCS220KE2 SBD SiC diode, as shown in Fig. 18(a).

TABLE V
MEASUREMENT PARAMETERS OF THE PROPOSED TRANSFORMER

	Self Inductor	Leakage Inductor	Voltage
Primary Side	184 μH	7.05 μH	800V(in)
Secondary Side 1	243.4 μH		870 V(out)
Secondary Side 2	243.6 μH	57.5 μH	873 V(out)
Secondary Side 3	243.3 μH		871 V(out)

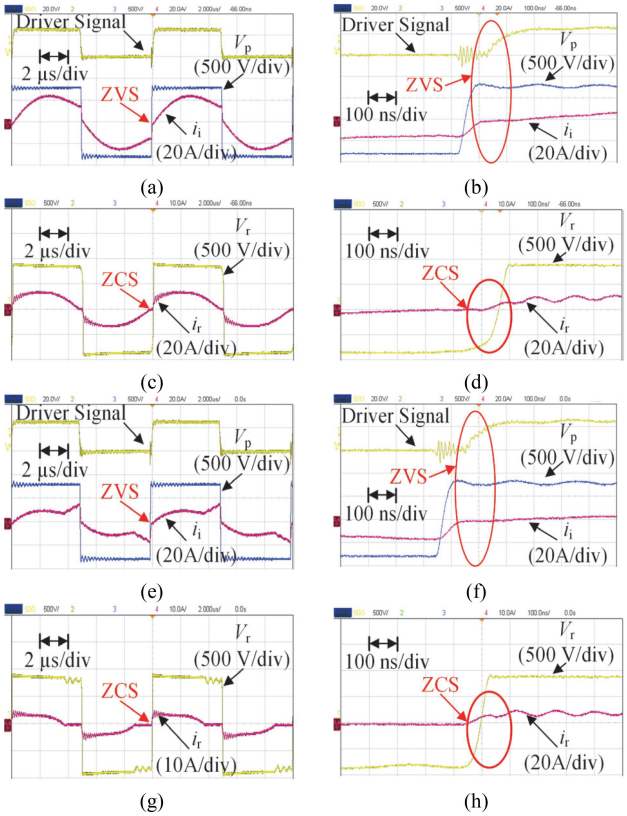

Fig. 19. Experimental waveforms for $P_{out} = 15$ kW. (a) V_p and i_i. (b) V_r and i_r and $P_{out} = 7.5$ kW. (c) V_p and i_i. (d) V_r and i_r.

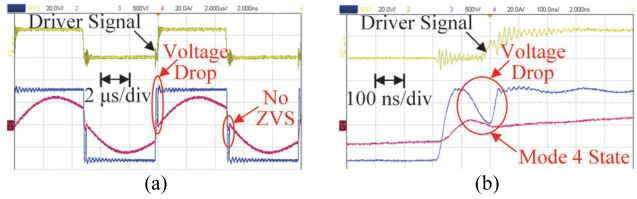

Fig. 20. Experimental waveforms for the appearance of Mode4.

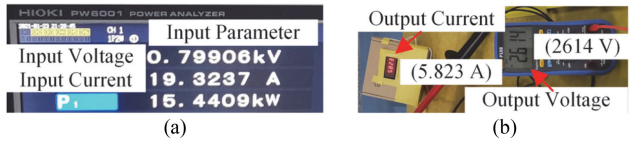

Fig. 21. Experimental results. (a) Input voltage parameters. (b) Output parameters.

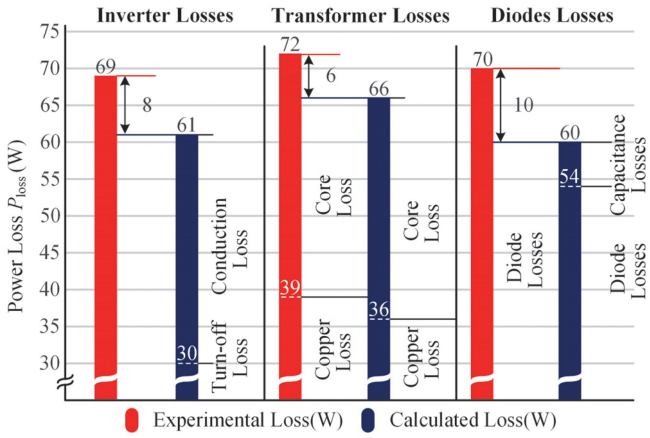

Fig. 22. Loss breakdown of the proposed module.

Each measured and simulated value parameters maintain an acceptable consistency shown in Table V. The actual manufacturer cannot make the transformer with perfect consistency with the FEM model. Moreover, the parameters of the material cannot be consistent. However, as long as the error of the calculated model is within the acceptable range, the actual transformer is available.

Fig. 19 shows the experimental waveforms under rated load (15 kW) and half load (7.5 kW). Fig. 19(a) and (c) shows that turn ON of ZVS is achieved for MOSFETs. Fig. 19(b) and (d) shows that ZCS is achieved for rectifiers. Furthermore, as the load becomes light, the turn-OFF time of the current in the secondary decreases. It is due to the rapid current increase caused by the junction capacitance of the diode.

Therefore, the current rapidly becomes zero under light load. Model 3 analyzes in detail the charging of this process. The detailed analysis process and optimization under light load are discussed in [36]. Moreover, Fig. 20 shows the appearance of Mode 4. Since the dead time is more significant than the calculated value, the current drops to zero when the MOSFETs are turned OFF. The current charges the capacitors of the MOSFETs again. If the MOSFETs are turned at this time, ZVS will be lost. It also leads to an increase of interference from the drive waveform.

Fig. 21 shows the results for input and output parameters. The power analyzer gives the input parameters of 15.44 kW. Due to the high output voltage limit, the three-digit precision battery-powered ammeter gives the output current. The output power is calculated as 15.22 kW. Then, the efficiency of the proposed system is calculated as 98.6%.

Loss breakdown under the rated load is analyzed in Fig. 22. The calculated loss is given by the loss model shown in Fig. 10. The direct measurement of the loss is not straightforward due to the high-frequency switching. Hence, the loss of each part can be obtained measured using a high-precision power analyzer of PW6001. Moreover, the transformer is placed in a thermostat to reach the rated operating temperature to separate the transformer's loss. Then, a high-frequency LCR meter is used to measure its ac resistance directly. In this way, the loss of the transformer can be separated. However, with the limit of the measuring devices, the inverter losses cannot be separated as

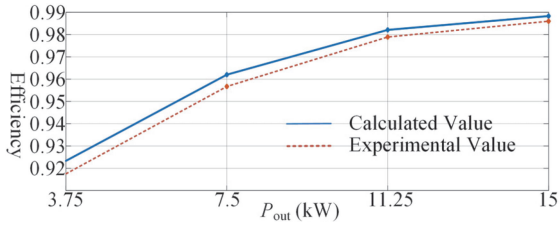

Fig. 23. Efficiency curve of calculated and experimental values.

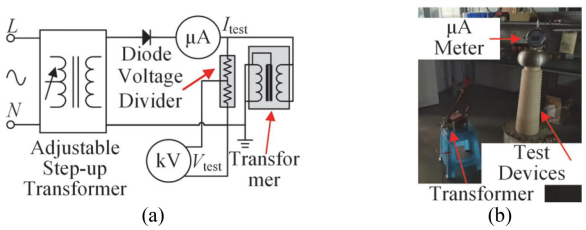

Fig. 24. Voltage insulation test. (a) Insulation test method. (b) Insulation test panorama.

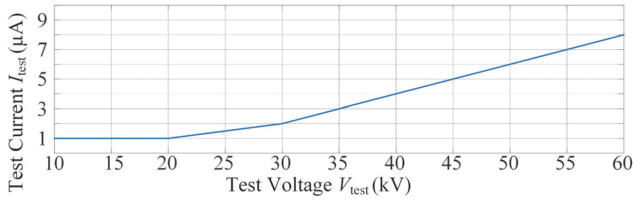

Fig. 25. Insulation test results.

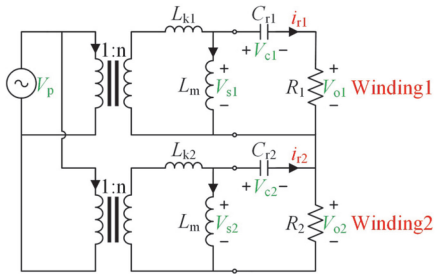

Fig. 26. Equivalent model of the two output windings.

turn-OFF loss and conduction loss. Moreover, the experimental losses are larger than the calculated loss. Three aspects have caused this deviation.

1) The PCB trace parameters are not taken into consideration.
2) The transformer losses ignore the influence of the edge magnetic flux. The temperature of the windings is regarded as uniform.
3) There is a deviation in the voltage drop parameters of the diode.

Nevertheless, the loss of the PCB is fixed. Therefore, the optimized data obtained by this model is acceptable.

Fig. 23 the efficiency trends of the calculated and experimental values are consistent under different load conditions. However, as the output power decreases, the deviation between the two values becomes larger. As the output power decreases, the fixed losses generated by the experimental platform, such as the PCB and connectors, take up a more significant percentage.

Fig. 24 shows the principle of the insulation test. It mainly uses the adjustable transformer to boost the line frequency voltage. It reads the indications of the microampere meter and the voltmeter to obtain the insulation test results. The voltage divider side and the step-up transformer negative pole should be well-grounded to ensure safety during the process. Besides, the converter's primary side and the magnetic core are grounded. The secondary side is connected to high voltage, satisfying the operating conditions. In Fig. 24(b), the test environment is dark, facilitating the observation of possible sparking during the process.

Fig. 25 shows the insulation test results of the transformer after the insulating material is potted. The result has passed the 60 kV voltage test for more than 3 m. The results show that the maximum current is 8 μA, which meets the insulation test requirements according to IEC 60073-3.

VI. Conclusion

An all-SiC IPOS isolated dc–dc converters for magnetron application was investigated in this article. The series-resonance added is presented with the turn ON of ZVS on the primary side and all-ZCS realization on the secondary side, considering the critical stray capacitance.

Furthermore, a three multioutput transformer is developed to realize output voltage sharing for the 1200 V SiC-SBD diodes. The proposed design and calculating methods are present with Pareto optimization. Moreover, an example presents the simulation and experimental results. The prototype fits the magnetron requirement and achieves a peak efficiency of 98.6%.

Appendix

A. Leakage Inductance Imbalance Analysis

To illustrate the effect of uneven winding leakage inductance, the equivalent model of the two windings is shown in Fig. 26.

In transformer fabrication, the manufacturer is focused on the number of turns to inspect and make. However, the leakage inductance of each winding allows for a certain amount of error.

On this basis, the analysis focuses on output voltage unbalance when the leakage inductance has deviated.

Winding 1 is assumed to be in resonance. The leakage inductance of Winding 2 has deviated. The amount of deviation of V_2 is used to measure this effect.

Thus, the load resistance R_L can be expressed as

$$R_{eq} = R_1 + R_2 = 8R_L/\pi^2. \tag{35}$$

According to Ohm's theorem, R_2 can be expressed as

$$R_2 = V_{o2}R_{eq}/\left(nV_p + V_{o2}\right). \tag{36}$$

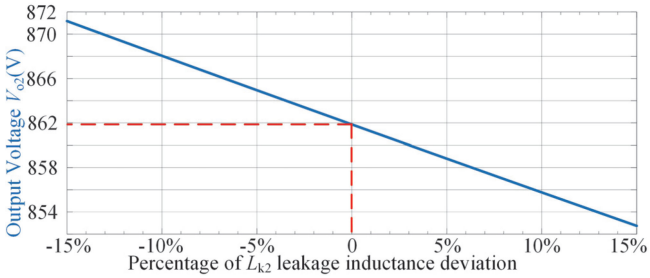

Fig. 27. Curve of output voltage variation with the deviation of leakage inductance.

Since the switching frequency operates near the resonant frequency, the FHA can be used for calculation. According to Kirchhoff's voltage theorem, V_{o2} can be expressed as

$$V_{o2} = \frac{nV_p}{j\omega L_{k2}} \frac{j\omega L_{k2} // j\omega L_m}{j\omega L_{k2} // j\omega L_m + 1/j\omega C + R_2} R_2. \quad (37)$$

Substituting (36) into (37), V_{o2} can be expressed as

$$V_{o2} = nV_p \frac{\left(\omega^2 C L_{k2} + j\omega C R_{eq} - 1\right) L_m - L_{k2}}{\left(-\omega^2 C L_{k2} + j\omega C R_{eq} + 1\right) L_m + L_{k2}\left(j\omega C R_{eq} + 1\right)}. \quad (38)$$

Taking the module operation for (38), V_{o2} can be expressed as

$$V_{o2} = nV_p \left(\sqrt{\begin{array}{l}(C L_m \omega)^2 \left({L_{k2}}^2 \omega^2 + {L_m}^2 {R_{eq}}^2\right) \\ -2C L_m L_{k2}\left(L_{k2} + L_m\right)\omega^2 + \left(L_{k2} + L_m\right)^2\end{array}} \Big/ \sqrt{\begin{array}{l}(C L_m \omega)^2 \left({L_{k2}}^2 \omega^2 + {L_m}^2 {R_{eq}}^2\right) \\ -2C L_m L_{k2}\left(L_{k2} + L_m\right)\omega^2 + \left(L_{k2} + L_m\right)^2 \\ +2L_m L_{k2}(C R_L \omega)^2 + \left(C L_{k2} R_L \omega\right)^2\end{array}} \right). \quad (39)$$

According to (39), the denominator below the root sign has two more terms than the numerator. The rest of the terms are equal. Therefore, V_{o2} negatively varies L_{k2} when the remaining parameters are constant. As shown in Fig. 27, the designed values are substituted (39) to give a more intuitive view of the variation law of V_{o2} with L_{k2}.

When leakage inductance deviates from 15%, the output voltage has a deviation of 10 V. However, due to the good uniformity of the leakage inductance, it is only about a 1% deviation in this article. Therefore, the output voltage deviation is less than 2 V. This is desirable in practical applications. As a result, all transformer secondary turns and leakage inductances are assumed to be equal to simplify the model.

B. Coefficients of the Time Domain Equation

$$A_1 = 2L_k\left(C_{oss} + n^2 C_{sr}\right) \quad \omega_1 = \sqrt{A_2/A_1}$$

$$A_2 = 2\left(L_k/L_m + \left(1/C_r + 1/C_{doss}\right)\left(C_{oss} + n^2 C_{sr}\right) - n^2\right)$$

$$A_3 = \left(\frac{1}{C_r} + \frac{1}{C_{doss}}\right)\frac{V_i}{3L_m t_{p1}} \quad A_4 = -\left(\frac{1}{C_r} + \frac{1}{C_{doss}}\right)\frac{V_i}{2L_m}$$

$$A_5 = -I_{m(1)}\left(1/C_r + 1/C_{doss}\right) \quad C_1 = A_6/A_2$$

$$A_6 = n\left(V_{Cr(1)} + V_o\right) - n^2 V_i - L_k V_i/L_m$$

$$C_2 = I_{m(1)}/2\omega_1\left(n^2 C_{sr} + C_{oss}\right) + A_5/A_2\omega_1$$

$$B_1 = 2L_k\left(C_{oss} + n^2 C_{sr}\right) \quad \omega_2 = \sqrt{B_2/B_1}$$

$$B_2 = 2\left(L_k/L_m + \left(1/C_r\right)\left(C_{oss} + n^2 C_{sr}\right) - n^2\right)$$

$$B_3 = V_i/\left(3L_m t_{p2} C_r\right) \quad B_4 = -V_i/\left(2L_m C_r\right)$$

$$B_5 = -I_{Lmh}/C_r \quad B_6 = n\left(V_{Cr(1)} - V_o\right) - n^2 V_i - L_k V_i/L_m$$

$$C_3 = B_6/B_2 + V_{Mc12} \quad C_4 = \frac{I_{m(2)} - nI_{r2}}{2\omega_3\left(n^2 C_{sr} + C_{oss}\right)} + \frac{B_5}{B_2\omega_3}.$$

REFERENCES

[1] M. Heggannavar and H. Kulkarni, "Design of magnetron power source from three phase supply," in *Proc. Int. Conf. Energy Syst. Appl.*, 2015, pp. 552–556.

[2] L. P. Pietta, M. E. Treter, J. S. Barin, and L. Michels, "Modelling and control of a high-frequency magnetron power supply for microwave heating applications," in *IEEE 13th Braz. Power Electron. Conf. 1st Southern Power Electron. Conf.*, 2015, pp. 1–6.

[3] M. Kim, W. Choi, I. Jeong, H. Park, and K. Park, "A new driving method of the magnetron power supply for a sulfur plasma lamp," *IEEE Trans. Ind. Electron.*, vol. 63, no. 9, pp. 5416–5424, Sep. 2016.

[4] S. Choi, I. Lee, and J. Lee, "Design of 5-kV/5-kW magnetron power supply using PWM SRC with PISO-Connected transformer," *IEEE Trans. Plasma Sci.*, vol. 46, no. 8, pp. 2840–2847, Aug. 2018.

[5] S. Jang, H. Ryoo, S. Ahn, J. Kim, and G. H. Rim, "Development and optimization of high-voltage power supply system for industrial magnetron," *IEEE Trans. Ind. Electron.*, vol. 59, no. 3, pp. 1453–1461, Mar. 2012.

[6] S. Lee, Y. Jeung, and D. Lee, "Output voltage regulation of IPOS modular dual active bridge DC/DC converters using sliding mode control," in *Proc. IEEE Appl. Power Electron. Conf. Expo.*, 2018, pp. 3062–3067.

[7] J. You, L. Cheng, B. Fu, and M. Deng, "Analysis and control of Input-parallel output-series based combined DC/DC converter with modified connection in output filter circuit," *IEEE Access*, vol. 7, pp. 58264–58276, 2019.

[8] M. Guan, "A series-connected offshore wind farm based on modular dual-active-bridge (DAB) isolated DC–DC converter," *IEEE Trans. Energy Convers.*, vol. 34, no. 3, pp. 1422–1431, Sep. 2019.

[9] R. Zhang, H. Xu, and Y. Wang, "A dynamic priority factor loop for fast voltage equalization applied to high power density DC–DC converter system," *IEEE Trans. Power Electron.*, vol. 35, no. 1, pp. 198–207, Jan. 2020.

[10] P. Hu, R. Yin, Z. He, and C. Wang, "A modular multiple DC transformer based DC transmission system for PMSG based offshore wind farm integration," *IEEE Access*, vol. 8, pp. 15736–15746, 2020.

[11] Y. Li, S. Shao, H. Chen, J. Zhang, and K. Sheng, "High-gain high-efficiency IPOS LLC converter with coupled transformer and current sharing capability," *CPSS Trans. Power Electron. Appl.*, vol. 5, no. 1, pp. 63–73, 2020.

[12] M. Daryaei, M. Ebrahimi, and S. A. Khajehoddin, "Alternative approach to analysis and design of series resonant converter at steady state," *IEEE Trans. Ind. Electron.*, vol. 66, no. 6, pp. 4424–4435, Jun. 2019.

[13] S. Tian, F. C. Lee, and Q. Li, "A simplified equivalent circuit model of series resonant converter," *IEEE Trans. Power Electron.*, vol. 31, no. 5, pp. 3922–3931, May 2016.

[14] W. Hsu, J. Chen, Y. Hsieh, and Y. Wu, "Design and steady-state analysis of parallel resonant DC–DC converter for high-voltage power generator," *IEEE Trans. Power Electron.*, vol. 32, no. 2, pp. 957–966, Feb. 2017.

[15] M. M. Ghahderijani, M. Castilla, A. Momeneh, J. T. Miret, and L. G. Vicuña, "Frequency-Modulation control of a DC/DC current-source parallel-resonant converter," *IEEE Trans. Ind. Electron.*, vol. 64, no. 7, pp. 5392–5402, Jul. 2017.

[16] Y. Cai, M. H. Ahmed, Q. Li, and F. C. Lee, "Optimal design of Megahertz LLC converter for 48-V bus converter application," *IEEE J. Emerg. Sel. Topics Power Electron.*, vol. 8, no. 1, pp. 495–505, Mar. 2020.
[17] M. H. Ahmed, F. C. Lee, and Q. Li, "Two-Stage 48-V VRM with intermediate bus voltage optimization for data centers," *IEEE J. Emerg. Sel. Topics Power Electron.*, vol. 9, no. 1, pp. 702–715, Feb. 2021.
[18] M. Li, Z. Ouyang, and M. A. E. Andersen, "High-Frequency LLC resonant converter with magnetic shunt integrated planar transformer," *IEEE Trans. Power Electron.*, vol. 34, no. 3, pp. 2405–2415, Mar. 2019.
[19] X. Zhao, C. Chen, J. Lai, and O. Yu, "Circuit design considerations for reducing parasitic effects on gan-Based 1-MHz high-power-density high-step-up/down isolated resonant converters," *IEEE J. Emerg. Sel. Topics Power Electron.*, vol. 7, no. 2, pp. 695–705, Jun. 2019.
[20] S. Jang, C. Yu, and H. Ryoo, "Trapezoidal approximation of LCC resonant converter and design of a multistage capacitor charger for a solid-state marx modulator," *IEEE Trans. Power Electron.*, vol. 33, no. 5, pp. 3816–3825, May 2018.
[21] M. Jaritz and J. Biela, "Onant converter for a solid state 2.88 MW/115-kV long pulse modulator," *IEEE Trans. Plasma Sci.*, vol. 42, no. 10, pp. 3014–3022, 2014.
[22] S. Mao, Y. Chen, C. Li, W. Li, J. Popovic, and J. A. Ferreira, "A coupled-inductor-based LCC resonant converter with the primary-parallel–secondary-series configuration to achieve output-voltage sharing for HV generator applications," *IEEE Trans. Power Electron.*, vol. 34, no. 7, pp. 6108–6122, Jul. 2019.
[23] L. Wu, L. Xiao, J. Zhao, and G. Chen, "Modelling and optimisation of planar matrix transformer for high frequency regulated LLC converter," *IET Power Electron.*, vol. 13, no. 3, pp. 516–524, 2020.
[24] Y. Liu *et al.*, "Quarter-Turn transformer design and optimization for high power density 1-MHz LLC resonant converter," *IEEE Trans. Ind. Electron.*, vol. 67, no. 2, pp. 1580–1591, Feb. 2020.
[25] C. Fei, F. C. Lee, and Q. Li, "High-Efficiency high-power-density LLC converter with an integrated planar matrix transformer for high-output current applications," *IEEE Trans. Ind. Electron.*, vol. 64, no. 11, pp. 9072–9082, Nov. 2017.
[26] Y. A. Wang and D. M. Xiao, "Prototype design for a high-voltage high-frequency rectifier transformer for high power use," *IET Power Electron.*, vol. 4, no. 6, pp. 615–623, 2011.
[27] S. Zhao, Q. Li, F. C. Lee, and B. Li, "High-Frequency transformer design for modular power conversion from medium-voltage AC to 400 VDC," *IEEE Trans. Power Electron.*, vol. 33, no. 9, pp. 7545–7557, Sep. 2018.
[28] M. A. Bahmani, E. Agheb, T. Thiringer, H. K. Hoidalen, and Y. Serdyuk, "Core loss behavior in high frequency high power transformers-I: Effect of core topology," *J. Renewable Sustain. Energy*, vol. 4, no. 3, 2012, Art. no. 033112.
[29] M. Kolincio, P. J. Chrzan, and P. Musznicki, "Multitransformer primary-side regulated flyback converter for supplying isolated IGBT and MOSFET drivers," *IEEE Trans. Ind. Electron.*, vol. 67, no. 2, pp. 1005–1012, Feb. 2020.
[30] L. Deng, P. Wang, X. Li, H. Xiao, and T. Peng, "Investigation on the parasitic capacitance of high frequency and high voltage transformers of multi-section windings," *IEEE Access*, vol. 8, pp. 14065–14073, 2020.
[31] M. Chanda, *Plastics Technology Handbook*. Boca Raton, FL, USA: CRC press, 2017.
[32] E. Agheb, M. A. Bahmani, H. K. Hoidalen, and T. Thiringer, "Core loss behavior in high frequency high power transformers-II: Arbitrary excitation," *J. Renewable Sustain. Energy*, vol. 4, no. 3, 2012, Art no. 033113.
[33] I. Villar, U. Viscarret, I. Etxeberria-Otadui, and A. Rufer, "Global loss evaluation methods for nonsinusoidally fed medium-frequency power transformers," *IEEE Trans. Ind. Electron.*, vol. 56, no. 10, pp. 4132–4140, Oct. 2009.
[34] T. Duerbaum and G. Sauerlaender, "Energy based capacitance model for magnetic devices," in *Proc. 16th Annu. IEEE Appl. Power Electron. Conf. Expo.*, 2001, pp. 109–115.
[35] C. Liu, L. Qi, X. Cui, Z. Shen, and X. Wei, "Wideband mechanism model and parameter extracting for high-power high-voltage high-frequency transformers," *IEEE Trans. Power Electron.*, vol. 31, no. 5, pp. 3444–3455, May 2016.
[36] Z. Fang *et al.*, "Energy feedback control of light-load voltage regulation for LLC resonant converter," *IEEE Trans. Power Electron.*, vol. 34, no. 5, pp. 4807–4819, May 2019.

Junkun Zhang was born in Hubei, China, in 1992. He received the B.S. degree from the Hubei Polytechnic University, Huangshi, China, in 2014, and the M.S. degree from the Wuhan University of Technology, Wuhan, China, in 2017, all in electrical engineering. He is currently working toward the Ph.D. degree with the Hunan University, Changsha, China.

In 2017, he was with the Institute of New Energy, Wuhan, where he is currently a Technique Supporting Executive. His research interests include inductive power transfer technology and dc–dc converters.

Bing Gao received the Ph.D. degree from the School of Electrical Engineering, Chongqing University, Chongqing, China, in 2016.

He is currently an Associate Professor with the College of Electrical and Information Engineering, Hunan University, Changsha. His research interests include the multiphysics coupling field calculation and digital twin for power electronics and the electro-acoustic device.

Zhixing He (Member, IEEE) was born in Hunan, China, 1989. He received the B.S. degree in information science and engineering from Central South University, Changsha, China, in 2011, and the Ph.D. degree in electrical engineering from Hunan University, Changsha, in 2017.

He was with the Hunan University, as Postdoctoral Researcher between 2017 and 2018. He is currently an Associate Professor with the College of Electrical and Information Engineering, Hunan University. His research interests include power electronics, medium voltage dc conversion, model predictive control, and modular multilevel converter.

Lei Wang (Senior Member, IEEE) received the B.Sc. degree in electrical and electronics engineering from the University of Macau (UM), Macao SAR, China, in 2011, the M.Sc. degree in electronics engineering from the Hong Kong University of Science and Technology, Hong Kong, in 2012, and the Ph.D. degree in electrical and computer engineering from UM, Macao SAR, China, in 2017.

From January 2017 to February 2019, he was a Postdoctoral Fellow with the Power Electronics Laboratory, UM. From February 2019 to August 2019, he was also a Visiting Fellow with the Department of Electrical and Computer Engineering, University of Auckland, Auckland, New Zealand. In 2019, he was with the College of Electrical and Information Engineering, Hunan University, Changsha, China, where he is currently a Full Professor. He has authored one Springer books, one Elsevier book chapter, five patents (USA and China) and more than 40 journal and conference papers.

Dr. Wang was the recipient of the champion award in the Schneider Electric Energy Efficiency Cup, Hong Kong, 2011, Macao Science and Technology R&D Award for Postgraduates (Ph.D) in 2018.

Renjie Hou was born in Shanxi, China, in 1997. He received the B.S. degree in electrical engineering and its automation from North University of China, Shanxi, China, in 2020. He is currently working toward the M.S. degree with Hunan University, Changsha, China.

His current research interests include medium voltage dc system and resonant dc converter.

Yang Liu was born in Hunan, China, 1997. He received the B.S. degree in electrical engineering and its automation in 2018 from Hunan University, Changsha, China, where he is currently working toward Ph.D. degree in electrical engineering with the College of Electrical and Information Engineering.

His main research interests include power electronics and medium voltage dc–dc conversion.

An Luo (Senior Member, IEEE) was born in Changsha, China, in 1957. He received the B.S. and M.S. degrees in industrial automation from Hunan University, Changsha, China, in 1982 and 1986, respectively, and the Ph.D. degree in fluid power transmission and control from Zhejiang University, Hangzhou, China, in 1993.

Between 1996 and 2002, he was a Professor with Central South University. Since 2003, he has been a Professor with the College of Electrical and Information Engineering, Hunan University, where he was the Chief of National Electric Power Conversion and Control Engineering Technology Research Center. His research interests mainly include distributed generation, microgrid, and power quality.

Prof. Luo was elected to the Chinese National Academy of Engineering in 2015, the highest honor for scientists and engineers and scientists in China. He has won the highly prestigious China National Science and Technology Awards three times (2014, 2010, and 2006).

Yandong Chen (Senior Member, IEEE) was born in Hunan, China, in 1979. He received the B.S. and M.S. degrees in instrument science and technology from Hunan University, Changsha, China, in 2003 and 2006, respectively, and the Ph.D. degree in electrical engineering from Hunan University, Changsha, China, in 2014.

He is currently a Professor with the College of Electrical and Information Engineering, Hunan University, Changsha, China. His research interests include power electronics for microgrid, distributed generation, power supply, and energy storage.

Dr. Chen was the recipient of the 2014 National Technological Invention Awards of China, and the 2014 WIPO-SIPO Award for Chinese Outstanding Patented Invention. He is a Senior Member of IEEE Power and Energy Society and IEEE Power Electronics Society.

Rong Han (Student Member, IEEE) was born in Gansu, China, in 1995. She received the B.S. degree in electrical engineering and automation in 2017 from Hunan University, Changsha, China, where she is currently working toward the Ph.D. degree in electrical engineering.

Her research interests include power conversion control, active thermal control, multilevel converters, and power quality control.